Title: Halide homogenization for low energy loss in 2-eV-bandgap perovskites and increased efficiency in all-perovskite triple-junction solar cells

Authors: Junke Wang[1,2,†], Lewei Zeng[1,†], Dong Zhang[2,3,†], Aidan Maxwell[1,†], Hao Chen[1,†], Kunal Datta[2], Alessandro Caiazzo[2], Willemijn H. M. Remmerswaal[2], Nick R. M. Schipper[2], Zehua Chen[4], Kevin Ho[5], Akash Dasgupta[6], Gunnar Kusch[7], Riccardo Ollearo[2], Laura Bellini[2], Shuaifeng Hu[6], Zaiwei Wang[1], Chongwen Li[1], Sam Teale[1], Luke Grater[1], Bin Chen[1,8], Martijn M. Wienk[2], Rachel A. Oliver[7], Henry J. Snaith[6], René A. J. Janssen[2,9,*], Edward H. Sargent[1,8,10*]

Affiliations:

[1]The Edward S. Rogers Department of Electrical and Computer Engineering, University of Toronto, Toronto, Ontario M5S 3G4, Canada

[2]Molecular Materials and Nanosystems, Institute for Complex Molecular Systems, Eindhoven University of Technology, partner of Solliance, P.O. Box 513, 5600 MB Eindhoven, The Netherlands

[3]TNO, partner of Solliance, High Tech Campus 21, Eindhoven, 5656 AE, The Netherlands

[4]Materials Simulation and Modelling, Department of Applied Physics, Eindhoven University of Technology, P.O. Box 513, 5600 MB Eindhoven, The Netherlands

[5]Department of Chemistry, University of Washington, Seattle, Washington 98195, United States

[6]Department of Physics, University of Oxford, Oxford OX1 3PU, United Kingdom

[7]Department of Materials Science and Metallurgy, University of Cambridge, Cambridge CB3 0FS, United Kingdom

[8]Department of Chemistry, Northwestern University, Evanston, Illinois 60208, United States

[9]Dutch Institute for Fundamental Energy Research, De Zaale 20, 5612 AJ Eindhoven, The Netherlands

[10]Department of Electrical and Computer Engineering, Northwestern University, Evanston, Illinois 60208, United States

*Email: r.a.j.janssen@tue.nl, ted.sargent@utoronto.ca

†These authors contributed equally

Abstract

Monolithic all-perovskite triple-junction solar cells have the potential to deliver power conversion efficiencies beyond those of state-of-art double-junction tandems and well beyond the detailed-balance limit for single-junctions. Today, however, their performance is limited by large deficits in open-circuit voltage and unfulfilled potential in both short-circuit current density and fill factor in the

wide-bandgap perovskite sub-cell. Here we find that halide heterogeneity – present even immediately following materials synthesis – plays, a key role in interfacial non-radiative recombination and collection efficiency losses under prolonged illumination, for Br-rich perovskites. We find that a diammonium halide salt, propane-1,3-diammonium iodide, introduced during film fabrication, improves halide homogenization in Br-rich perovskites, leading to significantly enhanced operating stability and a record open-circuit voltage of 1.44 V in an inverted (p-i-n) device; ~86% of the detailed-balance limit for a bandgap of 1.97 eV. The efficient wide-bandgap sub-cell enables the fabrication of monolithic all-perovskite triple-junction solar cells with an open-circuit voltage of 3.33 V and a champion PCE of 25.1% (NREL-certified 23.87%).

Main Text:

Integrating multiple absorber layers into a multijunction solar cell offers the ability to overcome the limitation of carrier thermalization from high-energy photons and transmission of low-energy photons observed in single-junction photovoltaics (PVs)[1]. Recent advances in metal halide perovskite semiconductors with bandgap energies from 1.2 to 1.8 eV have enabled their use in tandem solar cells with perovskite, crystalline silicon (c-Si), copper indium gallium selenide (CIGS), and organic photovoltaics (OPV)[2-6]. Among these, all-perovskite double-junction (2J) tandem solar cells coupling 1.77/1.22 eV absorbers have achieved a steady-state certified power conversion efficiency (PCE) of 29%[7]; higher than 26.1% for single-junction perovskite solar cells (PSCs)[8], indicative of the promise of perovskite PVs.

Pairing three perovskite junctions in a monolithic solar cell has the potential to lead to higher efficiencies compared to their 2J counterparts[9]. According to optical and device simulations, all-perovskite triple-junction (3J) solar cells featuring cascaded 2.0, 1.6, and 1.2 eV absorbers have a theoretical efficiency limit of >50% and could target PCE exceeding 36%[10,11]. However, only a limited number of studies have demonstrated 3J PSCs experimentally, and their realized performance remains lower than that of their single-junction and 2J counterparts[12-15].

Compared to their narrower-bandgap counterparts, inverted (p-i-n) single-junction PSCs of approximately 2 eV bandgap, typically produced by >60% Br contents, suffer from a large open-circuit voltage (V_{oc}) deficit of >700 mV (Fig. 1a,b) and performance loss as a consequence of light-induced halide segregation[16-18]. Recent studies have found that the dominant performance-limiting factors are increased band offset with charge transport layers and defect density in the wide-bandgap perovskite absorbers[19,20]. The latter is particularly evident for perovskites based on a high Br/I ratio, as they are susceptible to bulk and interfacial halide heterogeneity due to the uncontrolled growth of various halide species[21,22]. In addition to increased trap-mediated energy losses, defect sites can profoundly impact the charge-carrier dynamics of wide-bandgap perovskites when light-induced halide segregation occurs[23-28].

We sought to improve bulk and interfacial halide homogeneity in approximately 2 eV mixed Br/I perovskites in order to reduce energetic losses and better realize the potential of 3J PSCs. Previously, vacuum deposition has been utilized to produce uniform mixed-halide perovskites due to its superior compositional control[29]. For solution processing, the introduction of a Lewis acid–base adduct additive has been shown to regulate the crystallization of perovskites[30,31]; however, few studies have explored the impact of additives on the homogeneity of mixed Br/I perovskites[21,22]. In pursuing a pathway towards the phase homogenization of high-Br perovskite films with reduced defect densities, we turned to diammonium halide salts, which have been reported to have both a templating effect on perovskite growth as well as a capability to passivate surface defects[2,32-34]. We

show that a dual bulk and interface passivation technique with diammonium halide salts results in significantly suppressed non-radiative recombination within the perovskite bulk and at perovskite/charge-transporting-layer heterojunctions, enabling a record V_{oc} in a p-i-n device, ~86% of the detailed-balance (DB) limit at 1.97 eV. Interestingly, we observe that while the diammonium salt does not suppress light-induced halide segregation, wide-bandgap PSCs retain high operational stability (>28 hours) under prolonged illumination, beyond the stability of previous approximately 2 eV PSCs reported in literature[13,15,17]. We find that the additive promotes halide homogeneity near the buried perovskite/hole-transport-layer (HTL) interface and reduces trap-mediated recombination, collectively providing a pathway for efficient charge-carrier extraction from the halide-segregated regions. Encouraged by the stable and efficient wide-gap perovskite sub-cell, we fabricated all-perovskite 3J solar cells combining 1.97, 1.61, and 1.25 eV absorber layers. Using a front transparent conductive oxide (TCO) layer with high charge mobility and high near-infrared (NIR) transmittance, we demonstrate 3J devices with a V_{oc} of 3.33 V and a PCE of 25.1% (23.87% certified).

Wide-bandgap PSC performance and energy loss analysis

We developed a mixed-halide $Cs_{0.15}FA_{0.85}Pb(I_{0.4}Br_{0.6})_3$ perovskite composition alloyed using 5% $MAPbCl_3$ (FA = formamidinium, MA = methylammonium) to obtain a bandgap of 1.97 eV with desired surface morphology for multijunction applications (see Methods, Supplementary Figs. 1–3)[35,36]. To study energetic losses of such wide-bandgap perovskites in a p-i-n configuration, we first measured the quasi-Fermi level splitting (QFLS) by absolute photoluminescence (PL) spectroscopy of a series of perovskite films and half-stacks using NiO_x/[4-(3,6-dimethyl-9*H*-carbazol-9-yl)butyl]phosphonic acid (Me-4PACz)[37,38] as the HTL and [6,6]-phenyl-C_{61}-butyric acid methyl ester (PCBM) as electron transport layer (ETL) (Fig. 1a). Compared to the pristine wide-bandgap perovskite film deposited on glass (neat film), a 55 meV lower QFLS is measured for perovskites deposited on glass/indium tin oxide (ITO)/HTL substrates (w HTL), whereas a 114 meV QLFS loss is obtained for PCBM deposited atop the glass/perovskites (w ETL, Fig. 1c). This suggests that the perovskite/ETL interface is limiting the V_{oc} of wide-bandgap PSCs[37,39]. Similar to previous studies wherein diammonium cations have been shown to alter the surface potential of perovskites[2,33,40], we found that post-treatment of the perovskite with a solution of propane-1,3-diammonium iodide (PDA) salt effectively reduces the QFLS loss at the ETL interface to 45 meV, consistent with the V_{oc} improvement of full devices (Fig. 1d).

Interestingly, we found that the QFLS loss at the HTL (55 meV) is eliminated entirely upon addition of 1 mol% PDA into the perovskite precursor. This provides a lossless HTL interface as has previously been reported for perovskites of narrower bandgaps[2,37,41]. The top ETL interface shows a significantly reduced QFLS loss of 68 and 26 meV before and after surface treatment with PDA,

respectively. Leveraging these insights, we fabricated bulk and surface-passivated wide-bandgap PSCs using PDA, with a p-i-n structure of ITO/NiO_x/Me-4PACz/perovskite/PCBM/bathocuproine (BCP)/Ag. The PSCs achieved a V_{oc} of 1.44 V, reaching ~86% of the DB limit (Fig. 1b) at a 1.97 eV bandgap, as determined from the external quantum efficiency (EQE) spectrum (Supplementary Fig. 4); the highest reported for such solar cells (Fig. 1b)[16]. Combining a high fill factor (FF) of 0.83 and short-circuit current density (J_{sc}) of 12.8 mA cm^{-2}, the champion device has a PCE of up to 15.3% with negligible hysteresis and stable steady-state power output (Fig. 1d and Supplementary Fig. 5).

In addition to the performance enhancement, the PDA-modified wide-bandgap PSCs exhibit significantly improved operating stability. Under maximum point power point (MPP) tracking at 1 sun illumination, the control device (passivated by PDA only at the surface) dropped to below 90% of its initial performance after 0.5 h and ceased to be operational within 5 h, whereas the PCE of the PDA-modified device retained over 90% after 20 h (Fig. 1f). To our knowledge, this is the highest reported operating stability among mixed Br/I PSCs with a bandgap of approximately 2 eV, including their all-inorganic analogs[13,15,16]. We note that these hybrid perovskites also display superior ambient (ISOS D-1, Supplementary Fig. 6) and thermal stability (65 °C in N_2, Supplementary Fig. 7)[17]. For comparison, we also fabricated solar cells adding 1 mol% n-propylammonium iodide (PA), the monoammonium counterpart of PDA, in the perovskite and found an insignificant change in device stability. This suggests a synergistic effect of the two $–NH_3^+$ groups of PDA molecules in improving the performance of the wide-bandgap perovskites.

Photoinduced changes in wide-bandgap PSCs

To quantify the impact of halide segregation on the performance metrics under operating working conditions, we collected PL spectra in situ during current density-voltage (*J*–*V*) measurements on wide-bandgap PSCs (see Methods and Supplementary Figs. 8–9)[27].

In all cases, the initial PL peak attributed to the mixed-halide phase (~1.9 eV) diminished after ~10^3 s of illumination and was followed by a rise of a lower energy peak at ~1.6 eV (Figs. 2a–f). This has been attributed to the formation of lower bandgap I-rich perovskite domains into which charge carriers funnel and recombine radiatively[42]. Coincidently, the J_{sc} and FF of control and PA-added devices also diminish under continuous operation, leading to a severe loss of their initial PCEs between ~10^3 and 10^4 s (Fig. 2g and Supplementary Fig. 10). We consider that funneled charge carriers accumulate and recombine rapidly in the I-rich domains, rendering significant charge collection losses in the segregated device. This is supported by a significant increase in the rise and fall time during transient-photocurrent measurements, and dramatic shortening of the PL lifetime in the phase-segregated control and PA-modified samples (Fig. 2h and Supplementary Fig. 11)[24]. Notably, the relative loss in V_{oc} after halide segregation is much smaller, in agreement with previous

reports[20,27]. When we employ Mott–Schottky analysis (Supplementary Fig. 12), its account of loss in internal electric field is also minimal. We offer that light-induced halide segregation will mostly not affect charge selectivity and that interfacial carrier transport is little affected[43].

In contrast, the current extraction and carrier lifetime of PDA-modified perovskites are significantly less impacted by halide segregation. Although the PL intensity is enhanced by several orders of magnitude upon prolonged illumination (up to 10^5 s), PDA-modified devices show much slower degradation of photovoltaic performance, retaining ~75% of their initial PCE after ~28 h (10^5 s). Based on the above findings we infer that PDA additive promotes current extraction from the I-rich low-bandgap domains and improves the operating stability of wide-bandgap PSCs.

Formation kinetics of Br-rich wide-bandgap perovskites

To gain mechanistic insights into the role of PDA additive, we carried out detailed microstructural and compositional analysis for Br-rich wide-bandgap perovskites. The grazing-incidence wide-angle X-ray scattering (GIWAXS) patterns suggest that no low-dimensional perovskite or secondary phases are formed upon adding PDA into the perovskite films (Fig. 3a,b). The control and PDA-added perovskite films exhibit isotropic orientation of crystallites with a *q*-space value of 1.02 $Å^{-1}$ for the (100) Br-rich perovskite peak[44]. In addition, analysis of the XRD patterns and UV-vis spectra suggests that PDA does not significantly change the cubic lattice constant or bandgap of perovskite films (Fig. 3c,d and Supplementary Fig. 13). This implies that the PDA additive is not mixed into the perovskite crystal lattice[32,45]. Top-view scanning electron microscopy (SEM) images suggest that adding PDA slightly reduces the grain size of perovskite films (Supplementary Fig. 14). Photoinduced force microscopy (PiFM) and surface X-ray photoelectron spectroscopy (XPS) confirm that PDA additives are retained in the perovskite film (Supplementary Figs. 15–16). Compared to the control film, we also found that Pb 4*f*, I 3*d*, and Br 3*d* core-level peaks of PDA-added films are shifted toward lower binding energies (Supplementary Fig. 17). We infer that PDA possibly forms chemical bonds with the lead halide moieties near the perovskite grain boundaries, leading to a change in the electrostatic interaction between the Pb^{2+} and the halogen anions[40].

To study the impact of PDA on film formation kinetics, we performed in situ UV-vis absorption measurements during spin-coating and thermal annealing of wide-bandgap perovskite films (see Methods and Supplementary Fig. 18). Figs. 3e–f show that directly after dripping the antisolvent (at 39 s), an absorption onset near the 2.3 eV region appears and starts to redshift before the end of the process at ~45 s. This corresponds to the removal of excess solvent, and growth of perovskite nanocrystals with increased bandgap due to quantum confinement[21,46]. We found that for the as-cast control film, the absorption onset approaches ~2.15 eV, while for the as-cast 1 mol% PDA-added film, the absorption remains relatively low, with an onset above 2.20 eV (Fig. 3g). When the

PDA concentration is increased to 20 mol%, the absorption from any perovskite phase is suppressed without annealing (Fig. 3g and Supplementary Fig. 19). This confirms the capacity of PDA to interact with the perovskite precursors and slow the formation of perovskites during spin-coating. Furthermore, whereas annealing the control film at 100 °C immediately gives rise to the characteristic absorption spectra of mixed-halide wide-bandgap perovskites, PDA-added films exhibit delayed crystallization (Supplementary Figs. 20–21). This corresponds to an increased (100) peak intensity for up to 10 mol% PDA-added perovskite films; we propose that the delayed growth of perovskite produces more uniform film formation and higher crystallinity (Fig. 3c). We thus speculate that PDA enables controlled growth among halide species and facilitates homogeneous transformation to intermixed perovskite phases.

We performed XPS depth profile measurements to investigate the phase distribution of wide-bandgap perovskite films (Supplementary Fig. 22 and Fig. 3i). Interestingly, the control and PA-added films show the formation of a more Br-rich perovskite phase at the HTL interface. In comparison, the PDA-modified perovskite film is much more homogeneous, showing even distributions of halides (I, Br, and Cl) during sputtering. The results align with spatially resolved luminescence imaging, wherein a much narrower QFLS distribution and higher mean QFLS values are obtained for the PDA-added films toward the bottom interface (Supplementary Fig. 23). SEM cathodoluminescence (SEM-CL) hyperspectral imaging suggests that PDA-added films show less beam-induced ion migration and improved homogeneity at the microscopic scale (Supplementary Fig. 24). For mixed-halide perovskite precursors, density functional theory (DFT) calculations suggest that the formation of Br-based perovskite species is more thermodynamically favored than I-species, which results in large phase heterogeneity during a fast crystallization process (Supplementary Fig. 25). In comparison, PDA cations bind strongly to the interfaces of adjacent perovskite fragments, allowing more relaxation time for different halide ions to exchange and thereby the formation of uniform mixed-halide perovskite phases (Fig. 3h and Supplementary Note 1).

We discuss here the idea that, in control devices, heterogeneity generated prior to halide segregation occurs could induce a higher defect density towards the bottom interface, contributing to the non-radiative recombination losses at the perovskite/HTL interface. Chemical heterogeneity is correlated with lattice distortions and defective sites near the grain boundaries[47,48], further aggravating carrier trapping processes and shortening charge-carrier lifetimes as light-induced halide segregation now occurs in a more defective region (Supplementary Fig. 11)[25,27]. By contrast, PDA improves the halide homogeneity of perovskite films and eliminates detrimental interfacial losses in the presence of an HTL. Under illumination, PDA could therefore provide effective passivation around grain boundaries, reducing trap-mediated recombination and enabling more efficient current extraction of funneled charge carriers from the device. We note that further suppressing the light-

induced halide segregation by introducing lattice compression and distortion can increase device stability in Br-rich perovskite solar cells[15,49]. Further investigations of the compositional space of Br-rich hybrid organic-inorganic perovskite systems are thus of interest (Supplementary Fig. 26).

Monolithic all-perovskite 3J solar cell performance

Monolithic all-perovskite 3J solar cells comprising 1.97 eV wide-bandgap, 1.61 eV mid-bandgap $Cs_{0.05}FA_{0.9}MA_{0.05}Pb(I_{0.85}Br_{0.15})_3$, and 1.25 eV narrow-bandgap $Cs_{0.05}FA_{0.7}MA_{0.25}Pb_{0.5}Sn_{0.5}I_3$ absorbers were produced based on a device structure shown in Fig. 4a. A transparent hydrogenated indium oxide (IOH) front contact was used to reduce optical losses due to parasitic absorption in the NIR range[50] (Supplementary Fig. 27). The 1.97 and 1.61 eV sub-cells are connected through the PCBM/polyethyleneimine (PEI)/SnO_x/ITO/NiO_x/Me-4PACz recombination junction. Between the 1.61 and 1.25 eV sub-cells, a C_{60}/SnO_x/Au/poly(3,4-ethylene dioxythiophene):polystyrene (PEDOT:PSS) recombination junction was used[2,6]. We note that PCBM in the 1.97 eV sub-cell yields a higher V_{oc} than C_{60} due to reduced interfacial recombination losses (Supplementary Fig. 28)[51]. Here, the SnO_x layer was deposited by a temporal atomic layer deposition (ALD) process, and the PEI layer facilitates the nucleation of SnO_x atop the PCBM (Supplementary Fig. 29)[52]. In contrast to PEDOT:PSS, Me-4PACz provides a lossless HTL interface with 1.61 eV perovskites[37]. To ensure better coverage of Me-4PACz and thereby a shunt-free recombination junction, we used sputter-coated ITO and solution-processed NiO_x layers[38,50]. Enabled by the high performance of PDA-modified wide-bandgap sub-cells, the champion 3J device exhibits a high PCE of 25.1% (0.049 cm^2), with a V_{oc} of 3.33 V, a J_{sc} of 9.7 mA cm^{-2}, and FF of 0.78 (Fig. 4b). This high V_{oc} represents a 130-mV loss compared to the summed V_{oc} (3.47 V) of the single-junction PSCs. The 3J cells display stable operating performance, retaining 80% of their initial PCE after 200 hours of continuous MPP tracking under AM1.5G 1-sun illumination (Fig. 4g). Additionally, the 3J cell retained above 86% of its initial efficiency after more than 168 hours of storage at 65°C in N_2 (Supplementary Fig. 30). We also observed negligible hysteresis in the 3J devices (Supplementary Fig. 31). A statistical summary demonstrates good reproducibility of the 3J cells (Supplementary Fig. 32). For PDA-added 3J devices, a record efficiency of 23.87% was certified by NREL PV calibration laboratory using the asymptotic maximum power scan protocol[53]. The result outperforms the control (wide-bandgap perovskite passivated by PDA only at the surface) 3J device (21.49%), where lower cell metrics were recorded during the measurement (Fig. 4c and Supplementary Figs. 33–34).

Exploiting the full efficiency potential of all-perovskite 3J solar cells will require further reduction of optical losses and improved matching of the photo-generated current from all three sub-cells. Notably, the EQE-integrated J_{sc} was 12.6, 9.0, and 10.0 mA cm^{-2} for the wide-, mid-, and narrow-bandgap sub-cells, respectively, suggesting a large current mismatch of 3.6 mA cm^{-2}, with

the middle sub-cell limiting the J_{sc} of the 3J device (Fig. 4d). To explore the efficiency potential of all-perovskite 3J, we performed optical modeling using the transfer matrix (TM) method (Fig. 4e and Supplementary Figs. 35–36) and reconstructed the *J*–*V* characteristics of the triple cell by scaling the *J*–*V* curves of reference single-junction devices to the J_{sc} from simulated EQE, and adding their voltages at each current value (considering a 130 mV V_{oc} loss)[54]. Fine-tuning the thickness of perovskite absorbers and implementing more optically transparent layers (such as ITO and NiO_x/SAM[50,55]) should reduce the current mismatch and parasitic absorption losses of the narrow-bandgap sub-cell (Supplementary Figs. 37–39). This enables a J_{sc} of ~11 mA cm^{-2} in the 3J device and improves the PCE to 29.7%, which surpasses existing state-of-the-art all-perovskite 2J solar cells[7]. Here, we highlight the importance of enhancing optical responses to advance the PCE of 3J devices, and note that this J_{sc} is above previous estimates from simulation work[11] wherein impractical perovskite layer thicknesses were used. We note, however, that simply increasing the bandgap by adding more Br or Cl in the 1.97 eV perovskite could result in larger surface roughness and lower device performance (Supplementary Figs. 2–3 and 40–41). Further device engineering is required in order to retain high performance and stability after reducing the thickness or increasing the bandgap of the wide-bandgap perovskite absorbers.

Furthermore, we anticipate that the V_{oc} of each sub-cell equaling ~95% of its DB limit is feasible through optimizations of the perovskite absorber and the limiting perovskite/charge-transporting layer interfaces. As such, a V_{oc} of 3.71 V can be expected in the 3J device (considering a 100-mV loss). Ultimately, combining a J_{sc} of 11.0 mA cm^{-2} and an FF of 0.83 should enable a PCE of 33.7%, exceeding the DB limit for single-junction solar cells and simulations[10,11]. Overall, our experimental results and calculations demonstrate the immense potential of all-perovskite 3J devices.

Conclusions

We reported a strategy to enhance the performance and operating stability of Br-rich wide-bandgap PSCs. Incorporating the diammonium PDA molecule into Br-rich perovskites has enabled controlled film growth from solution, and improved halide homogeneity. Benefiting from the passivation effect of PDA near grain boundaries, Br-rich wide-bandgap PSCs retain fast charge collection processes and significantly improved stability under prolonged illumination. The PDA-added perovskites have effectively suppressed energetic losses at the perovskite/charge-transporting layer interfaces, leading to a record V_{oc} of 1.44 V at a bandgap of 1.97 eV. Combining 1.97, 1.61, and 1.25 eV perovskite sub-cells, we fabricated record monolithic all-perovskite triple-junction solar cells with an in-lab PCE of 25.1% (certified 23.87%) with a high V_{oc} of 3.33 V. Guided by optical simulation, we have demonstrated a route for all-perovskite 3J devices to surpass state-of-the-art all-perovskite tandem technologies and further to achieving a PCE approaching the DB limit.

Methods

Materials. All materials were purchased from suppliers and used without purification unless stated otherwise. Patterned glass substrates (3×3 cm^2) with ITO were purchased from Naranjo Substrates. CsI (99.999%), PbI_2 (99.99%), $PbBr_2$ (>98.0%), $PbCl_2$ (>99.0%), and Me-4PACz (>99.0%) were purchased from TCI Chemicals. Organic halides, including FAI, MAI, MABr, MACl, $PDAI_2$ (≥98%), PAI, and 4-fluoro-phenethylammonium bromide (4F-PEABr), were purchased from Greatcell Solar Materials. SnI_2 (99.99), SnF_2 (99%), glycine hydrochloride (99%), guanidine thiocyanate (GuaSCN, 99%), PEI solution (M_n ~60,000 g mol^{-1}, M_w ~750,000 g mol^{-1}, 50 wt% in H_2O), ethane-1,2-diammonium iodide ($EDAI_2$, 98%), and all anhydrous solvents were purchased from Sigma-Aldrich. PCBM (99%) was purchased from Nano-C. PEDOT:PSS (Al 4083) was purchased from Heraeus Clevios. C_{60} and BCP were purchased from Xi'an Polymer Light Technology.

Perovskite precursor solutions. Wide-bandgap perovskite precursor solutions were prepared by dissolving 1 M CsI (0.15), PbI_2 (0.1), $PbBr_2$ (0.9), FAI (0.85), $PbCl_2$ (0.053), MACl (0.053) in *N*,*N*-dimethylformamide (DMF, anhydrous 99.8%) and dimethyl sulfoxide (DMSO, anhydrous 99.9%) at a volume ratio of 4:1. PAI or $PDAI_2$ (1–20 mol%) was added to the precursor solution. Mid-bandgap perovskite precursor solutions were prepared by dissolving 1.5 M CsI (0.05), PbI_2 (0.8), $PbBr_2$ (0.2), FAI (0.9), MABr (0.05) in DMF and DMSO at a volume ratio of 4:1. Narrow-bandgap perovskite precursor solutions were prepared by dissolving 1.8 M CsI (0.05), PbI_2 (0.5), SnI_2 (0.5), SnF_2 (0.05), FAI (0.7), MAI (0.25), GuaSCN (4 mg mL^{-1}), 4F-PEABr (2 mg mL^{-1}), glycine hydrochloride (4 mg mL^{-1}), and Sn powder (5 mg mL^{-1}) in DMF and DMSO at a volume ratio of 3:1. All the solutions were stirred at 60 °C for 1 h and filtered by 0.22 μm PTFE syringe filter before use.

Device fabrication. Glass/ITO or Glass/IOH substrates were sequentially cleaned with acetone, soapy water, deionized water, 2-propanol, and 30 min of UV-ozone before use. For both wide-bandgap and mid-bandgap single-junction perovskite solar cells, NiO_x nanoparticles (prepared following a previously reported method[38], 5 mg mL^{-1} at a 3:1 volume ratio of H_2O and 2-propanol) were spin-coated on the substrates at 3000 rpm for 30 s (1000 rpm s^{-1} acceleration) in the air without any post-treatment. The substrates were then transferred into a N_2 glovebox, where Me-4PACz solution (0.3 mg mL^{-1} in ethanol) was spin-coated at 3000 rpm for 30 s (1000 rpm s^{-1} acceleration) and annealed at 100 °C for 10 min. After cooling, wide-bandgap perovskite precursor solution was dropped onto the substrate and spin-coated at 1000 rpm for 10 s (500 rpm s^{-1} acceleration) and 5000 rpm for 30 s. 150 μL anisole was dropped onto the substrate at 5 s before the end. The perovskite precursor film was immediately annealed at 100 °C for 10 min. After cooling, the $PDAI_2$ solution (0.5 mg mL^{-1} in 2-propanol/CB at a volume ratio of 2:1) was dynamically spin-coated on the perovskite film at 4000 rpm for 30 s and annealed at 100 °C for 5 min. Afterward, for wide-bandgap perovskites, PCBM (15 mg mL^{-1} in chlorobenzene, CB) was spin-coated at 1000 rpm for 30 s (1000 rpm s^{-1} acceleration) while 20 nm C_{60} was evaporated onto the mid-bandgap perovskites, before depositing 8 nm BCP and 140 nm Ag on top by thermal evaporation.

For Pb-Sn narrow-bandgap perovskite solar cells, PEDOT:PSS (diluted in IPA at a volume ratio of 1:2) was spin-coated on the substrate at 4000 rpm for 30 s and annealed at 120 °C for 10 min in air. The substrates were then transferred to a N_2 glovebox, on which perovskite precursor solution was spin-coated at 1000 rpm for 10 s (200 rpm s^{-1}) and 3800 rpm for 45 s (1000 rpm s^{-1}). 300 µL CB was dropped at 18 s before the end. The perovskite precursor film was immediately annealed at 100 °C for 10 min. $EDAI_2$ (0.5 mg mL^{-1} dissolved in 2-propanol:toluene at a volume ratio of 4:3) at 4000 rpm for 25 s (1300 rpm s^{-1}) and annealed at 100 °C for 5 min. Afterward, 20 nm of C_{60}, 8 nm of BCP, and 140 nm of Ag were deposited sequentially by thermal evaporation.

For all-perovskite 3J solar cells: The single-junction perovskite absorbers were prepared as previously described. Between wide- and mid-bandgap perovskite sub-cells, after depositing PCBM, PEI solution (0.025 wt% diluted in 2-propanol) was spin-coated at 4000 rpm for 30 s (2000 rpm s^{-1} acceleration) without any post-treatment. 20 nm of ALD-SnO_x was then deposited on top and followed by sputtering of 20 nm ITO. Between mid- and narrow-bandgap perovskite sub-cells, 20 nm of ALD-SnO_x was deposited on C_{60} and followed by 1 nm of Au by thermal evaporation before spin-coating PEDOT:PSS in the air. Shadow masks were used to ensure that only active areas were covered with ITO and Au to avoid shunt losses. Instead of BCP, 20 nm of ALD-SnO_x was deposited atop narrow-bandgap perovskite and C_{60}.

Device characterizations. *J–V* measurements were performed in a N_2 atmosphere at room temperature, using a solar simulator (Newport, Class A) with a light intensity of 100 mW cm^{-2} (calibrated by a reference solar cell from Newport) and a Keithley 2400 source meter. The voltage was scanned from the V_{oc} to the J_{sc} (reverse) and from the J_{sc} to the V_{oc} (forward) directions with a scanning rate of 100 mV s^{-1} (voltage step of 10 mV). The active area was determined by the aperture mask (0.049 cm^2). A spectral mismatch of 1.0 was used for all measurements. For stability measurements, solar cells were operated at the maximum power point and measured the output current, using G2V Sunbrick with a simulated AM1.5G 1-sun illumination. EQE measurements were performed in ambient air (Enlitech). For 3J solar cells, LED bias light (735+940 nm for 1.97 eV wide sub-cell, 470+940 nm for 1.61 eV mid sub-cell, and 470+735 nm for 1.25 eV narrow sub-cell) and bias voltage equivalent to the summed V_{oc} of optically biased sub-cells were applied to measure the EQE response of each sub-cell[54].

For in situ PL and *J–V* measurements[27], wide-bandgap PSCs were sealed in a nitrogen-filled box with a quartz window and connected to a Keithley 2400 source meter. A green LED (Thorlabs M530L3, 530 nm), filtered by a 600 nm short pass filter, was used to illuminate the device at a 1-sun equivalent light intensity such that the solar cell initially generates a photocurrent equal to the J_{sc} under simulated AM1.5G illumination. The PL light, filtered by a 590 nm long pass filter, was focused on an optical fiber and recorded using a spectrometer (Avantes Avaspec-2048x14). Firstly, the solar cell was held at the V_{oc}, and a PL spectrum was recorded with an integration time of 100 ms from a spot in the active area of the solar cell. This is followed by a reverse voltage sweep from +1.5 to –0.1 V and a forward voltage sweep from –0.1 to +1.5 V at a scan rate of 120 mV

s^{-1} (voltage step of 16 mV). Afterward, the solar cell was held at a voltage bias close to the maximum power point under illumination for a certain delay before starting the next PL and *J*–*V* measurement.

The Mott–Schottky analysis was performed by measuring the capacitance–voltage (*C*–*V*) characteristics of solar cells using an electrochemical station (Solartron SI1260 impedance/gain-phase analyzer) in an N_2 box under a dark condition. The capacitance was measured by sweeping the voltage (DC) from –0.5 V to 3.0 V. The frequency was kept at 10 kHz with a perturbation voltage of 10 mV.

Film characterizations. Absolute PL measurements were performed using an integrating sphere (Avantes, AvaSphere-30-REFL) installed in a N_2 glovebox, where a 455 nm LED (Thorlabs M455F3-455 fiber coupled LED source) was used to excite the perovskite film (at ~1 sun equivalent intensity) through an optical fiber fitted with a 550 nm short pass filter. The spectra were measured through an optical fiber connected to a calibrated AvaSpec-HERO spectrometer (Avantes) using a 550 nm long pass filter. XRD patterns were recorded by a Bruker D2 Phaser diffractometer equipped with Cu Kα radiation (λ = 1.5405 Å). GIWAXS measurements were performed at the BXDS (LE-wiggler) beamline of the Canadian Light Source (CLS) using X-rays of a wavelength of λ = 0.84 Å, at a grazing incidence angle of 1.0°. Ex situ UV-vis absorption spectra were acquired by PerkinElmer Lamda 900 UV-vis-NIR spectrophotometer. Surface and depth profile XPS measurements were measured using a Thermo Scientific K-Alpha with a 180° double-focusing hemispherical analyzer and a 128-channel detector. A monochromatic Al Kα radiation (1486.6 eV) was used, and the X-ray spot size was 400 μm. For the sputtering experiments, the perovskite/HTL sample was removed layer-by-layer using argon ion etching operated at mid-current and ion energy of 3000 eV. A snapshot mode was used for each element with the number of frames 5×1 s.

In situ UV-vis absorption measurements were performed in a N_2 glovebox during spin-coating and thermal annealing[56]. The backside of the glass substrates was painted with white paint and dried before UV-ozone treatment. The substrate was placed on a spin coater or a hot plate and illuminated by a white light from a halogen lamp. A fiber optical cable was placed at an off-specular angle which collects the light scattered from the paint and transmitted through the as-cast film. The fiber was connected to a spectrometer and the absorption spectra can be calculated using $A(\lambda) = -log_{10}(\frac{I_m(\lambda)-I_{m,dark}(\lambda)}{I_{m,blank}(\lambda)-I_{m,dark}(\lambda)})$, where I_{m}, $I_{\mathrm{m,dark}}$, and $I_{\mathrm{m,blank}}$ represent wavelength-dependent photon counts of the sample during measurement, the dark reference before turning on the lamp, and a blank reference for an empty substrate with white paint, respectively.

CL hyperspectral maps were acquired in an Attolight Allalin 4027 Chronos in continuous wave mode, at room temperature and under a high vacuum. All secondary electron (SE) images and CL maps were acquired at 3 kV acceleration voltage, approximately 63 pA beam current, and 128 × 128 pixels resolution in a 3.14 μm field of view. CL intensities over specific energy ranges were integrated to generate energy bandpass-filtered images.

The luminescence imaging and QFLS mapping were performed by a previously reported method[57]. A 440 nm LED (Thorlabs, M450LP1) was used to illuminate perovskite films deposited on glass substrates at either the front or the back surfaces. The photon flux was calibrated at ~1 sun intensity for wide-bandgap perovskites (Multicomp PRO MP710086 bench power supply). An imaging camera (Andor Zyla 4.2 sCMOS sensor) equipped with a Kowa LM50XC lens (50 mm lens with up to an F2.0 aperture) to acquire the PL images.

Photoinduced force microscopy was collected with a Molecular Vista instrument coupled to a QCL laser. The images and spectra were collected using the sideband mode with a PPP-NCHAu gold coated AFM Probe from Nanosensors.

DFT calculations. Ab initio molecular dynamic simulations (AIMD) were performed with CP2K code[58]. We used the mixed Gaussian and plane-wave method (QUICKSTEP formalism) and the Perdew-Burke-Ernzerhof exchange-correlation functional (PBE) within the generalized gradient approximation (GGA)[59,60]. The van der Waals interactions through the DFT-D3 scheme[61] were included to account for dispersion interactions. The Gaussian basis set employed for all atoms is a double-ζ polarized basis set with polarization functions in conjunction with the Goedecker-Teter-Hutter (GTH) pseudopotentials[62,63]. To investigate the possible ammonium cation-perovskite interactions, we constructed PDA-perovskite interface, PDA-perovskite surface, and PA-perovskite surface models, respectively. As the FA cation is the dominant A cation in experimentally fabricated perovskite films, we thus only, to reduce the complexity, consider the interaction modes of PDA and PA with $FAPbX_3$ (X = I or Br). A constant-pressure and constant-temperature (NPT) ensemble was used for the interface model whereas for surface model we used a constant-volume and constant-temperature (NVT) ensemble. The temperature was controlled with a Nose-Hoover thermostat[64] at room temperature (300 K). Each simulation was run for 10 ps to ensure equilibrium and the time step was set to 1.0 fs. The plane-wave cutoff for the expansion of the electron density was set to 300 Ry. The convergence criteria on forces were set at 4.5×10^{-4} Har/Bohr (0.02 eV/Å). We observe in the AIMD simulations that the halide anions tend to escape from the perovskite surface in the PDA-perovskite surface model. The PDA-perovskite surface model is thus not considered in further calculations.

The binding energies (E_b) of ammonium cations with the perovskite interface or surface are defined as $E_b = E_{mol/pvsk} - E_{pvsk} - E_{mol}$, where $E_{mol/pvsk}$, E_{pvsk}, and E_{mol} are the total energies of the ammonium cation-perovskite crystal system, the perovskite system after removing an ammonium halide compound ($PDAX_2$/PAX, X = I or Br), and the ammonium-halide compound, respectively. Here, the ammonium cation-perovskite systems are taken from the snapshots of the AIMD equilibrium simulations. The atomic positions of these systems are optimized further by CP2K code at the ground state.

To calculate the formation energy of the perovskite cluster, we constructed the cubic supercell of 20 × 20 × 20 Å with a cluster in the center of the cell. Atomic positions of the cluster are optimized by the Vienna ab initio simulation package (VASP)[65]. The formation energies (E_f) of perovskite cluster with respect to the corresponding binary species is defined as $E_f = E_c(AX{:}PbX_2) - E_c(AX) - E_c(PbX_2)$, where $E_c(AX{:}PbX_2)$,

$E_c(AX_2)$, and $E_c(PbX_2)$ are the total energies of perovskite cluster, AX (A = FA, Cs; X = I, Br) cluster, and BX_2 cluster, respectively.

Optical simulations. Optical modeling was performed with GenPro4 program[66]. The optical constants of wavelength-dependent refractive indices and extinction coefficient of all layers were measured individually by depositing corresponding materials on silicon and characterized with a J.A. Wollam ellipsometer.

Data availability

All data generated or analyzed during this study are included in the published article and its Supplementary Information and Source Data files. Further data that support the findings of this study are available from the corresponding authors on reasonable request.

Acknowledgements

We thank David Ginger and Fangyuan Jiang of the University of Washington for facilitating the PiFM and discussions on PL mapping experiments. This work was partly supported by the Ontario Research Fund Research Excellence programme (ORF7: Ministry of Research and Innovation, Ontario Research Fund-Research Excellence Round 7). This work was also supported by the King Abdullah University of Science and Technology under award no. OSR-2020-CRG9-4350.2. The authors from the Eindhoven University of Technology acknowledge funding by The Netherlands Organization for Scientific Research (NWO) through the Joint Solar Programme III (Project 680.91.011) and the Spinoza prize awarded to R.A.J. Janssen and by the Ministry of Education, Culture and Science (Gravity program 024.001.035). The authors also acknowledge Solliance, a partnership of R&D organizations from The Netherlands, Belgium, and Germany working in thin-film photovoltaic solar energy. J.W. and R.A.J. Janssen acknowledge funding from the EU's Horizon Europe research and innovation under Grant Agreement No. 101075605 (SuPerTandem). K.H. acknowledges the Dept. of Energy, Basic Energy Sciences DE-SC0013957 for supporting his PiFM microscopy work in support of the project. A.D. would like to thank the Penrose Scholarship for funding his studentship. R.A.O. and G.K. acknowledge financial support from the Engineering and Physical Sciences Research Council (EPSRC) (under EP/R025193/1). S.H. and H.S. acknowledge funding from the EU's Horizon Europe research and innovation program under grant agreement No. 101075330 (NEXUS). H.S. also acknowledges funding from the EPSRC UK under EP/S004947/1. The authors thank the Canadian Light Source (CLS) for support through a travel grant. GIWAXS patterns were collected at the BXDS Beamline at the CLS with the assistance of Dr. Adam Leontowich and Dr. Chang-Yong Kim. The CLS is funded by NSERC, the Canadian Institutes of Health Research, Canada Foundation for Innovation, the Government of Saskatchewan, Western Economic Diversification Canada, and the University of Saskatchewan. We thank Tao Song for efficiency certification in NREL.

Author contributions

J.W., L.Z., D.Z., M.W., R.J., and E.S. planned the research and analyzed the results. J.W. and L.Z. fabricated the triple-junction cells. J.W., L.Z., H.C., A.M., and C.L. prepared the triple cells for certifications. J.W. optimized the wide-bandgap sub-cells and coordinated all the characterization of materials and devices. H.C. optimized the mid-bandgap sub-cell. A.M. and C.L. optimized the narrow-bandgap sub-cell. W.R. performed the absolute PL and QFLS analysis. K.D. developed and helped measure the in situ PL/$J-V$ characteristics and wrote the LabVIEW code. A.C. performed the XPS and in situ absorption measurements. L.Z., N.S. and L.B. fabricated and characterized perovskite thin films for stability. Z.C. performed DFT calculations. K.H. performed PiFM and analyzed the data. A.D. performed luminescence mapping and analysis. S.H. helped analyze the XRD data and crystallization dynamics. H.S. facilitated and supervised the luminescence imaging experiments. G.K. and R.A.O. carried out the SEM-CL measurements and analysis. R.O. performed the transient photocurrent measurements. S.T. and L.G. performed the GIWAX measurements. D.Z. performed optical simulations and provided the IOH substrates for triple-junction cells. Z.W. and B.C. provided valuable suggestions for optimizing the wide-bandgap sub-cell and 3J device configurations. J.W. wrote the first manuscript, and all authors commented on it. E.S. and R.J. supervised the project.

Competing interests

H.S. is cofounder and CSO of Oxford PV Ltd. All other authors declare no competing interests.

Additional information

Supplementary Information accompanies this paper.

Fig. 1 | Photovoltaic performance of 1.97 eV wide-bandgap PSCs. a, Inverted (p-i-n) device structure. **b**, Bandgap-dependent V_{oc} for p-i-n single-junction PSCs with a PCE above 5%. The cell data was acquired from an open-access perovskite database[16]. In the plot, the DB limit (solid line), 90% of the DB limit (dashed line), the highest V_{oc} of this work (solid star), and reported cell data (open brackets) are shown. **c**, QFLS of control and 1 mol% PDA-added perovskite films deposited on glass (neat), with PCBM on top (w ETL), and on ITO/NiO_x/Me-4PACz (w HTL). The perovskite samples (unpassivated) are further post-treated with a PDA solution on the top surface (passivated). **d**, J–V characteristics (reverse scans) of single-junction 1.97 eV PSCs without (control, green) and with 1 mol% PDA addition (purple) in the perovskite bulk. The top surface of unpassivated perovskites (dashed lines) was treated with PDA (passivated, solid lines) on top. **e**, EQE spectrum of the best-performing PSC. The J_{sc} (12.7 mA cm^{-2}) was obtained by integrating with the AM1.5G spectrum. **f**, Stabilized MPP tracking of encapsulated control, PA-, and PDA-modified PSCs at room temperature in the air under simulated AM1.5G 1-sun illumination condition. The initial performance of each device is displayed in Supplementary Fig. 5. Note that all the perovskite surfaces were passivated.

Fig. 2 | Photostability and cell performance of 1.97 eV wide-bandgap PSCs during in situ PL and J–V measurements. Time-resolved PL intensity maps under a 530 nm LED illumination at one-sun equivalent intensity for **a**, the control (~2.8 h), **b**, 1 mol% PA- (~16 h), and **c**, 1 mol% PDA-modified (~28 h) PSCs measured at the V_{oc}, and selected PL spectra at different time intervals for **d**, the control, **e**, PA-, and **f**, PDA-modified devices. **g**, Evolution of the photovoltaic parameters (V_{oc}, J_{sc}, FF, and PCE) under reverse scans and the PL intensities of 1.6–1.7 eV (I-segregated) phases for

1.97 eV PSCs under illumination. **h**, The rise (left) and fall (right) time (μs) extracted from transient-photocurrent measurements for the control, PA-, and PDA-modified PSCs.

Fig. 3 | Structure, composition, and formation kinetics of Br-rich wide-bandgap perovskite films. GIWAX patterns of **a**, the control and **b**, 1 mol% PDA-added perovskite films. **c**, XRD patterns and **d**, cubic lattice parameters and bandgap at varying PDA concentrations (0–20 mol%). To exclude the influence of halide on the lattice constant and optical bandgap, stoichiometric $PDAI_2$, $PDABr_2$, and $PDACl_2$ were used. Time-resolved absorption intensity maps during spin-coating of **e**, control, and **f**, 1 mol% PDA-added perovskite precursor solutions. The antisolvent anisole was dropped onto the spinning substrate at ~39 s. **g**, The absorption spectra of perovskite precursor films after the spin-coating and after 50 s of thermal annealing at 100 °C. **h**, Schematics of PDA cation and mixed Br/I perovskite precursors during the crystallization process. **i**, The ratio of atomic concentrations between halide (Br, I, and Cl) and Pb atoms obtained from XPS depth profiles for the control (solid lines) and PDA-added (dashed lines) perovskite films. The dashed vertical line is a guide to show the interface with the HTL.

Fig. 4 | Photovoltaic performance and simulations of monolithic all-perovskite triple-junction solar cells. a, Device configuration of optimized 3J cell stack. **b**, *J–V* characteristics of the representing 1.97, 1.61, and 1.25 eV, as well as the champion 3J solar cells. **c**, NREL-certified *J–V* characteristics of 3J devices using a control (green) and PDA-modified (orange) 1.97 eV sub-cells. **d**, EQE spectra of 1.97 (12.6 mA cm^{-2}), 1.61 (9.0 mA cm^{-2}), and 1.25 (10.0 mA cm^{-2}) eV sub-cells in a 3J solar cell. **e**, EQE spectra of 1.97 (10.9 and 11.0 mA cm^{-2}), 1.61 (10.8 and 11.0 mA cm^{-2}), and 1.25 (10.2 and 11.0 mA cm^{-2}) eV sub-cells after thickness optimizations to approach a current-matched condition (dashed lines) and after using optically transparent recombination junction (solid lines). A total EQE spectrum (gray dotted line) represents the summed EQE of all three sub-cells. In both Fig. 4d and e, the J_{sc} was obtained by integrating with the AM1.5G spectrum. **f**, Experimental and reconstructed *J–V* characteristics of the 3J device from the simulated EQE at different optical conditions and assuming a V_{oc} of 95% of the detailed-balance limit was achieved in each sub-cell. **g**, MPP tracking stability of an encapsulated 3J device in the air at room temperature under simulated AM1.5G 1-sun illumination. The initial performance is displayed in Supplementary Fig. 30. T_{80} is the time for device stability to reduce to 80% of its initial PCE.

References

1. Shockley, W., Queisser H. J. Detailed Balance Limit of Efficiency of p-n Junction Solar Cells. *J. Appl. Phys.* **32**, 510–519 (1961).
2. Chen, H., et al. Regulating surface potential maximizes voltage in all-perovskite tandems. *Nature* **613**, 676–681 (2023).
3. Tockhorn, P., et al. Nano-optical designs for high-efficiency monolithic perovskite–silicon tandem solar cells. *Nat. Nanotechnology* **17**, 1214–1221 (2022).
4. Jošt, M., et al. Perovskite/CIGS Tandem Solar Cells: From Certified 24.2% toward 30% and Beyond. *ACS Energy Lett.* **7**, 1298−1307 (2022).
5. Brinkmann, K. O., et al. Perovskite–organic tandem solar cells with indium oxide interconnect. *Nature* **604**, 280−286 (2022).
6. Lin, R., et al. All-perovskite tandem solar cells with improved grain surface passivation. *Nature* **603**, 73−78 (2022).
7. Green, M. A., et al. Solar cell efficiency tables (version 62). *Prog. Photovolt. Res. Appl.* **31**, 651–663 (2023).
8. NREL Chart, https://www.nrel.gov/pv/assets/pdfs/best-research-cell-efficiencies.pdf. (August 2023).
9. Martí, A., Araújo G. L. Limiting efficiencies for photovoltaic energy conversion in multigap systems. *Sol. Energ. Mater. Sol. Cells* **43**, 203–222 (1996).
10. Eperon, G. E., Hörantner M. T., Snaith H. J. Metal halide perovskite tandem and multiple-junction photovoltaics. *Nat. Rev. Chem.* **1**, 0095 (2017).

11. Hörantner, M. T., et al. The Potential of Multijunction Perovskite Solar Cells. *ACS Energy Lett.* **2**, 2506–2513 (2017).
12. Wang, J., Zardetto V., Datta K., Zhang D., Wienk M. M., Janssen R. A. J. 16.8% Monolithic all-perovskite triple-junction solar cells via a universal two-step solution process. *Nat. Commun.* **11**, 5254 (2020).
13. Xiao, K., et al. Solution-Processed Monolithic All-Perovskite Triple-Junction Solar Cells with Efficiency Exceeding 20%. *ACS Energy Lett.* **5**, 2819−2826 (2020).
14. McMeekin, D. P., et al. Solution-Processed All-Perovskite Multi-junction Solar Cells. *Joule* **3**, 387–401 (2019).
15. Wang, Z., et al. Suppressed phase segregation for triple-junction perovskite solar cells. *Nature* **618**, 74–79 (2023).
16. Jacobsson, T. J., et al. An open-access database and analysis tool for perovskite solar cells based on the FAIR data principles. *Nat. Energy* **7**, 107−115 (2022).
17. Yang, T. C.-J., Fiala P., Jeangros Q., Ballif C. High-Bandgap Perovskite Materials for Multijunction Solar Cells. *Joule* **2**, 1421–1436 (2018).
18. Zhao, Y., et al. Strain-activated light-induced halide segregation in mixed-halide perovskite solids. *Nat. Commun.* **11**, 6328 (2020).
19. Stolterfoht, M., et al. The impact of energy alignment and interfacial recombination on the internal and external open-circuit voltage of perovskite solar cells. *Energy Environ. Sci.* **12**, 2778−2788 (2019).
20. Mahesh, S., et al. Revealing the origin of voltage loss in mixed-halide perovskite solar cells. *Energy Environ. Sci.* **13**, 258–267 (2020).
21. Huang, T., et al. Performance-limiting formation dynamics in mixed-halide perovskites. *Sci. Adv.* **7**, eabj1799 (2021).
22. Correa-Baena, J.-P., et al. Homogenized halides and alkali cation segregation in alloyed organic-inorganic perovskites. *Science* **363**, 627–631 (2019).
23. Peña-Camargo, F., et al. Halide Segregation versus Interfacial Recombination in Bromide-Rich Wide-Gap Perovskite Solar Cells. *ACS Energy Lett.* **5**, 2728–2736 (2020).
24. Motti, S. G., Patel J. B., Oliver R. D. J., Snaith H. J., Johnston M. B., Herz L. M. Phase segregation in mixed-halide perovskites affects charge-carrier dynamics while preserving mobility. *Nat. Commun.* **12**, 6955 (2021).
25. Knight, A. J., Patel J. B., Snaith H. J., Johnston M. B., Herz L. M. Trap States, Electric Fields, and Phase Segregation in Mixed-Halide Perovskite Photovoltaic Devices. *Adv. Energy Mater.* **10**, 1903488 (2020).
26. Barker, A. J., et al. Defect-Assisted Photoinduced Halide Segregation in Mixed-Halide Perovskite Thin Films. *ACS Energy Lett.* **2**, 1416–1424 (2017).
27. Datta, K., et al. Effect of Light-Induced Halide Segregation on the Performance of Mixed-Halide Perovskite Solar Cells. *ACS Appl. Energy Mater.* **4**, 6650−6658 (2021).
28. Macpherson, S., et al. Local nanoscale phase impurities are degradation sites in halide perovskites. *Nature* **607**, 294–300 (2022).
29. Gil-Escrig, L., et al. Efficient Wide-Bandgap Mixed-Cation and Mixed-Halide Perovskite Solar Cells by Vacuum Deposition. *ACS Energy Lett.* **6**, 827–836 (2021).
30. Li, C., et al. Rational design of Lewis base molecules for stable and efficient inverted perovskite solar cells. *Science* **379**, 690–694 (2023).
31. Taddei, M., et al. Ethylenediamine Addition Improves Performance and Suppresses Phase Instabilities in Mixed-Halide Perovskites. *ACS Energy Lett.* **7**, 4265–4273 (2022).
32. Ke, W., et al. Ethylenediammonium-Based "Hollow" Pb/Sn Perovskites with Ideal Band Gap Yield Solar Cells with Higher Efficiency and Stability. *J. Am. Chem. Soc.* **141**, 8627−8637 (2019).
33. Hu, S., et al. Optimized carrier extraction at interfaces for 23.6% efficient tin–lead perovskite solar cells. *Energy Environ. Sci.* **15**, 2096–2107 (2022).
34. Yan, N., et al. Ligand-Anchoring-Induced Oriented Crystal Growth for High-Efficiency Lead-Tin Perovskite Solar Cells. *Adv. Funct. Mater.* **32**, 2201384 (2022).
35. Moot, T., et al. Choose Your Own Adventure: Fabrication of Monolithic All-Perovskite Tandem Photovoltaics. *Adv. Mater.* **32**, 2003312 (2020).
36. Xu, J., et al. Triple-halide wide-band gap perovskites with suppressed phase segregation for efficient tandems. *Science* **367**, 1097–1104 (2020).
37. Al-Ashouri, A., et al. Monolithic perovskite/silicon tandem solar cell with >29% efficiency by enhanced hole extraction. *Science* **370**, 1300–1309 (2020).
38. Chen, H., et al. Quantum-size-tuned heterostructures enable efficient and stable inverted perovskite solar cells. *Nat. Photonics* **16**, 352–358 (2022).

39. van Gorkom, B. T., van der Pol T. P. A., Datta K., Wienk M. M., Janssen R. A. J. Revealing defective interfaces in perovskite solar cells from highly sensitive sub-bandgap photocurrent spectroscopy using optical cavities. *Nat. Commun.* **13**, 349 (2022).
40. Cheng, L., et al. Highly Thermostable and Efficient Formamidinium-Based Low-Dimensional Perovskite Solar Cells. *Angew. Chem. Int. Ed.* **60**, 856−864 (2021).
41. Caprioglio, P., et al. Open-circuit and short-circuit loss management in wide-gap perovskite p-i-n solar cells. *Nat. Commun.* **14**, 932 (2023).
42. Andaji-Garmaroudi, Z., et al. A Highly Emissive Surface Layer in Mixed-Halide Multication Perovskites. *Adv. Mater.* **31**, 1902374 (2019).
43. Ravishankar, S., Liu Z., Rau U., Kirchartz T. Multilayer capacitances: How selective contacts affect capacitance measurements of perovskite solar cells. *PRX Energy* **1**, 013003 (2022).
44. Noel, N. K., et al. Highly Crystalline Methylammonium Lead Tribromide Perovskite Films for Efficient Photovoltaic Devices. *ACS Energy Lett.* **3**, 1233–1240 (2018).
45. Eperon, G. E., et al. The Role of Dimethylammonium in Bandgap Modulation for Stable Halide Perovskites. *ACS Energy Lett.* **5**, 1856−1864 (2020).
46. Taylor, A. D., et al. A general approach to high-efficiency perovskite solar cells by any antisolvent. *Nat. Commun.* **12**, 1878 (2021).
47. Doherty, T. A. S., et al. Performance-limiting nanoscale trap clusters at grain junctions in halide perovskites. *Nature* **580**, 360−366 (2020).
48. Jones, T. W., et al. Lattice strain causes non-radiative losses in halide perovskites. *Energy Environ. Sci.* **12**, 596−606 (2019).
49. Muscarella, L. A., et al. Lattice Compression Increases the Activation Barrier for Phase Segregation in Mixed-Halide Perovskites. *ACS Energy Lett.* **5**, 3152–3158 (2020).
50. Datta, K., et al. Monolithic All-Perovskite Tandem Solar Cells with Minimized Optical and Energetic Losses. *Adv. Mater.* **34**, 2110053 (2022).
51. Liu, Z., Siekmann J., Klingebiel B., Rau U., Kirchartz T. Interface Optimization via Fullerene Blends Enables Open-Circuit Voltages of 1.35 V in $CH_3NH_3Pb(I_{0.8}Br_{0.2})_3$ Solar Cells. *Adv. Energy Mater.* **11**, 2003386 (2021).
52. Palmstrom, A. F., et al. Enabling Flexible All-Perovskite Tandem Solar Cells. *Joule* **3**, 2193−2204 (2019).
53. Song, T., Friedman D. J., Kopidakis N. Comprehensive Performance Calibration Guidance for Perovskites and Other Emerging Solar Cells. *Adv. Energy Mater.* **11**, 2100728 (2021).
54. Di Carlo Rasi, D., Hendriks K. H., Wienk M. M., Janssen R. A. J. Accurate Characterization of Triple-Junction Polymer Solar Cells. *Adv. Energy Mater.* **7**, 1701664 (2017).
55. Kapil, G., et al. Tin–Lead Perovskite Solar Cells Fabricated on Hole Selective Monolayers. *ACS Energy Lett.* **7**, 966–974 (2022).
56. Wang, J., et al. Understanding the Film Formation Kinetics of Sequential Deposited Narrow-Bandgap Pb–Sn Hybrid Perovskite Films. *Adv. Energy Mater.* **10**, 2000566 (2020).
57. Dasgupta, A., et al. Visualizing Macroscopic Inhomogeneities in Perovskite Solar Cells. *ACS Energy Lett.* **7**, 2311–2322 (2022).
58. Hutter, J., Iannuzzi M., Schiffmann F., VandeVondele J. cp2k: atomistic simulations of condensed matter systems. *WIREs Comput. Mol. Sci.* **4**, 15–25 (2014).
59. VandeVondele, J., Krack M., Mohamed F., Parrinello M., Chassaing T., Hutter J. Quickstep: Fast and accurate density functional calculations using a mixed Gaussian and plane waves approach. *Comput. Phys. Comm.* **167**, 103–128 (2005).
60. Perdew, J. P., Burke K., Ernzerhof M. Generalized Gradient Approximation Made Simple. *Phys. Rev. Lett.* **77**, 3865–3868 (1996).
61. Grimme, S., Antony J., Ehrlich S., Krieg H. A consistent and accurate ab initio parametrization of density functional dispersion correction (DFT-D) for the 94 elements H-Pu. *J. Chem. Phys.* **132**, 154104 (2010).
62. VandeVondele, J., Hutter J. Gaussian basis sets for accurate calculations on molecular systems in gas and condensed phases. *J. Chem. Phys.* **127**, 114105 (2007).
63. Goedecker, S., Teter M., Hutter J. Separable dual-space Gaussian pseudopotentials. *Phys. Rev. B* **54**, 1703–1710 (1996).
64. Nosé, S. A unified formulation of the constant temperature molecular dynamics methods. *J. Chem. Phys.* **81**, 511–519 (1984).
65. Kresse, G., Furthmüller J. Efficient iterative schemes for ab initio total-energy calculations using a plane-wave basis set. *Phys. Rev. B* **54**, 11169–11186 (1996).

66. Santbergen, R., Meguro T., Suezaki T., Koizumi G., Yamamoto K., Zeman M. GenPro4 Optical Model for Solar Cell Simulation and Its Application to Multijunction Solar Cells. *IEEE J. Photovolt.* **7**, 919–926 (2017).

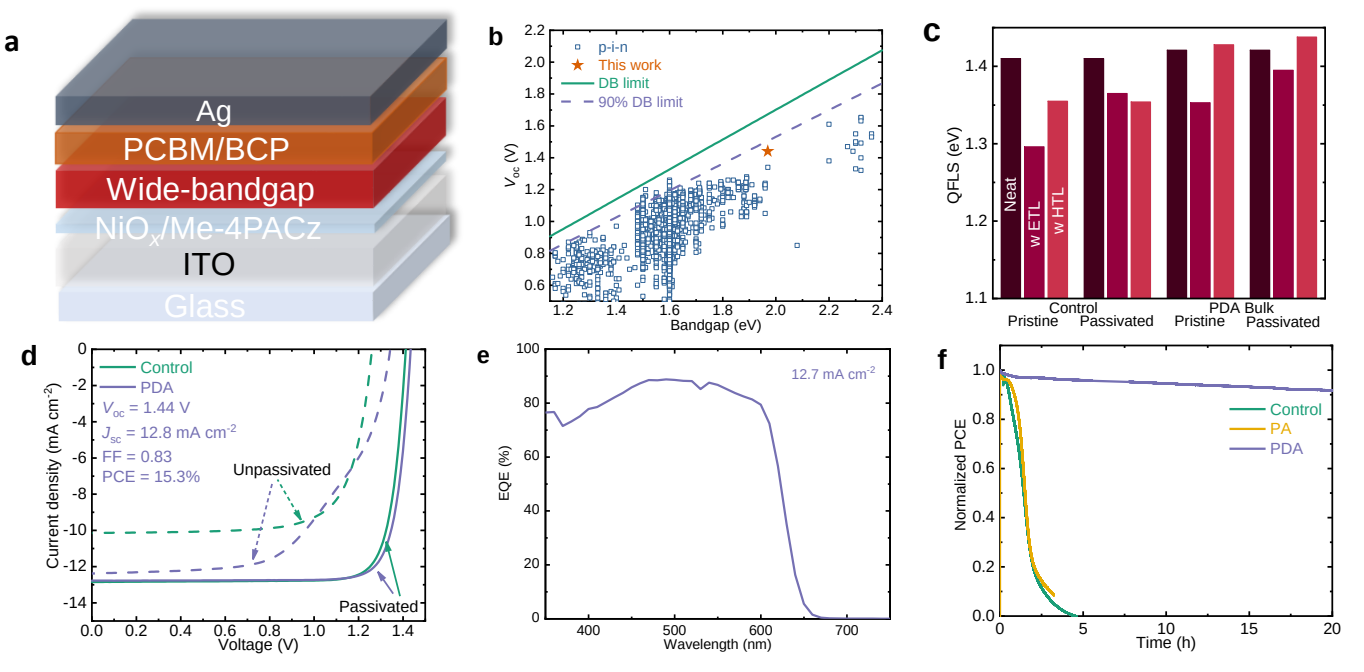
a
Ag
PCBM/BCP
Wide-bandgap
NiOx/Me-4PACz
ITO
Glass
b
p-i-n
This work
DB limit
90% DB limit
Voc (V)
Bandgap (eV)
c
QFLS (eV)
Neat
w ETL
w HTL
Control
Pristine
Passivated
PDA Bulk
Pristine
Passivated
d
Control
PDA
Voc = 1.44 V
Jsc = 12.8 mA cm-2
FF = 0.83
PCE = 15.3%
Unpassivated
Passivated
Current density (mA cm-2)
Voltage (V)
e
12.7 mA cm-2
EQE (%)
Wavelength (nm)
f
Control
PA
PDA
Normalized PCE
Time (h)

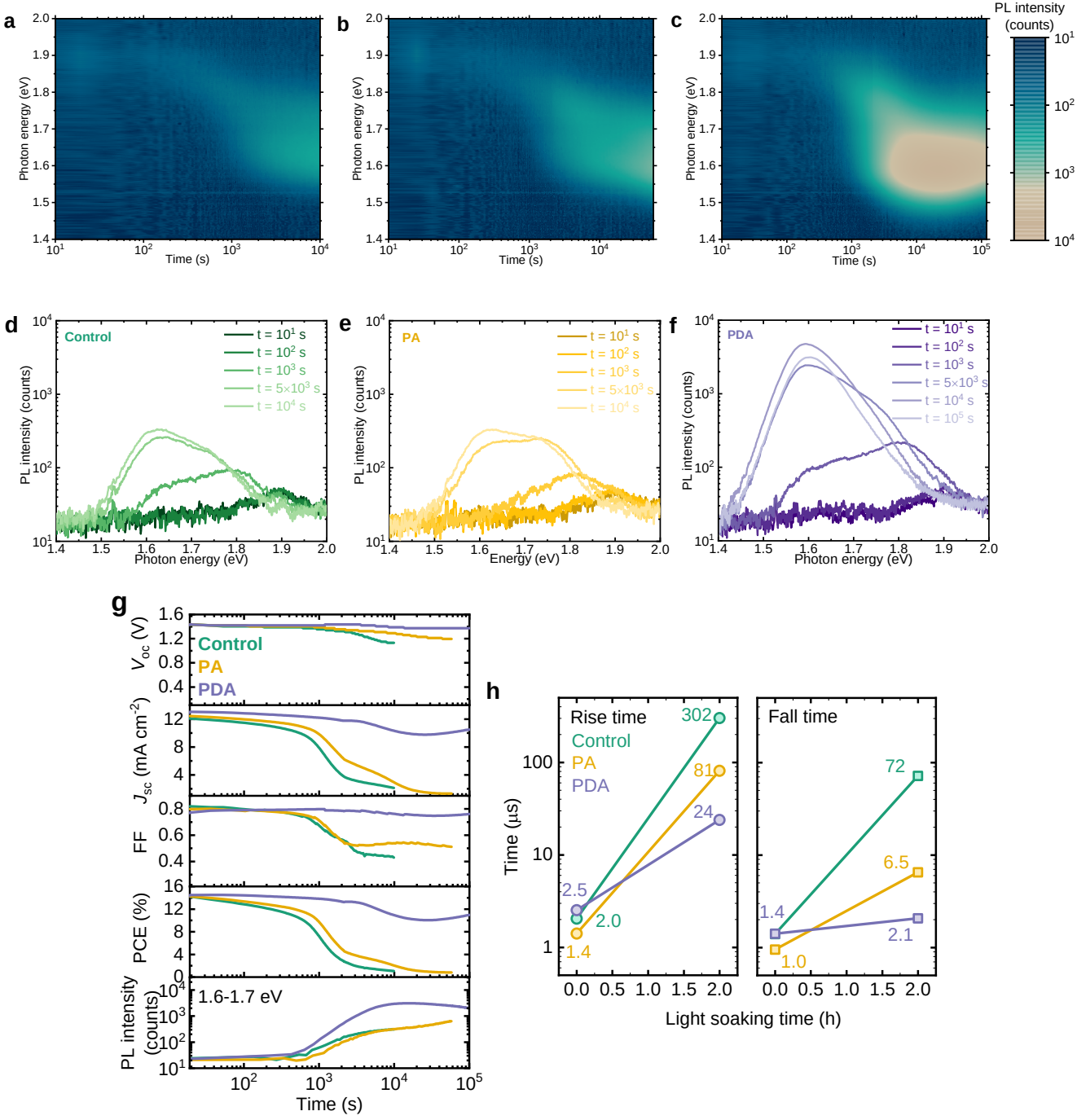
a
b
c
Photon energy (eV)
Time (s)
PL intensity (counts)
d
e
f
Control
PA
PDA
t = 10^1 s
t = 10^2 s
t = 10^3 s
t = 5×10^3 s
t = 10^4 s
t = 10^5 s
PL intensity (counts)
Photon energy (eV)
Energy (eV)
g
h
Control
PA
PDA
V_oc (V)
J_sc (mA cm^-2)
FF
PCE (%)
PL intensity (counts)
1.6-1.7 eV
Time (s)
Rise time
Fall time
Time (μs)
Light soaking time (h)
302
81
24
2.5
2.0
1.4
72
6.5
1.4
2.1
1.0

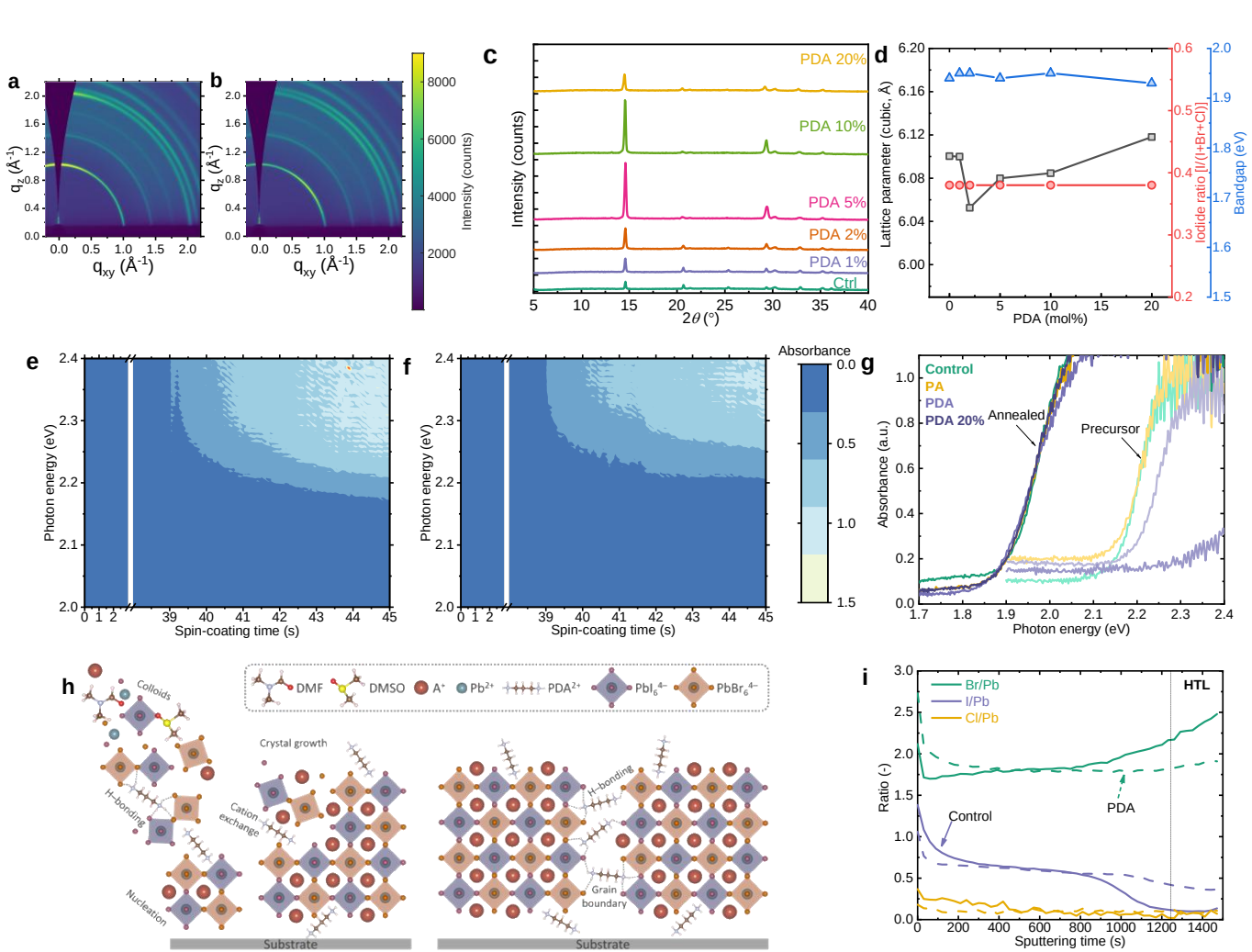
a
b
c
d
e
f
g
h
i
q_z (Å^{-1})
q_{xy} (Å^{-1})
Intensity (counts)
PDA 20%
PDA 10%
PDA 5%
PDA 2%
PDA 1%
Ctrl
2θ (°)
Lattice parameter (cubic, Å)
Iodide ratio I/(I+Br+Cl)
Bandgap (eV)
PDA (mol%)
Photon energy (eV)
Spin-coating time (s)
Absorbance
Control
PA
PDA
PDA 20%
Annealed
Precursor
Absorbance (a.u.)
DMF
DMSO
A$^+$
Pb^{2+}
PDA^{2+}
PbI$_6^{4-}$
PbBr$_6^{4-}$
Colloids
H-bonding
Nucleation
Crystal growth
Cation exchange
Substrate
π–π bonding
Grain boundary
Substrate
Br/Pb
I/Pb
Cl/Pb
HTL
Control
PDA
Ratio (-)
Sputtering time (s)

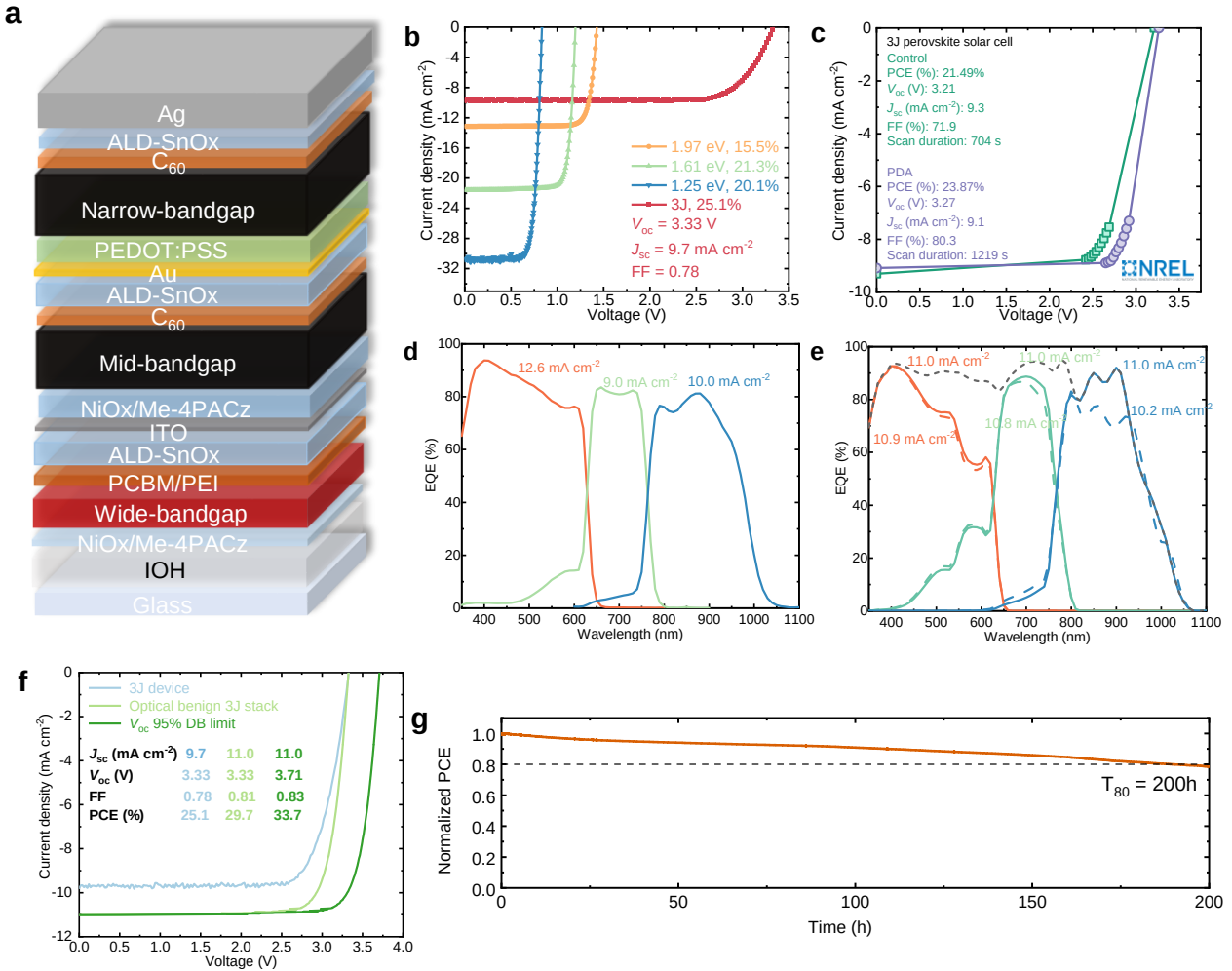
a
Ag
ALD-SnOx
C60
Narrow-bandgap
PEDOT:PSS
Au
ALD-SnOx
C60
Mid-bandgap
NiOx/Me-4PACz
ITO
ALD-SnOx
PCBM/PEI
Wide-bandgap
NiOx/Me-4PACz
IOH
Glass
b
Current density (mA cm-2)
Voltage (V)
1.97 eV, 15.5%
1.61 eV, 21.3%
1.25 eV, 20.1%
3J, 25.1%
Voc = 3.33 V
Jsc = 9.7 mA cm-2
FF = 0.78
c
3J perovskite solar cell
Control
PCE (%): 21.49%
Voc (V): 3.21
Jsc (mA cm-2): 9.3
FF (%): 71.9
Scan duration: 704 s
PDA
PCE (%): 23.87%
Voc (V): 3.27
Jsc (mA cm-2): 9.1
FF (%): 80.3
Scan duration: 1219 s
NREL
d
EQE (%)
Wavelength (nm)
12.6 mA cm-2
9.0 mA cm-2
10.0 mA cm-2
e
11.0 mA cm-2
11.0 mA cm-2
11.0 mA cm-2
10.2 mA cm-2
10.9 mA cm-2
10.8 mA cm-2
f
3J device
Optical benign 3J stack
Voc 95% DB limit
Jsc (mA cm-2) 9.7 11.0 11.0
Voc (V) 3.33 3.33 3.71
FF 0.78 0.81 0.83
PCE (%) 25.1 29.7 33.7
g
Normalized PCE
Time (h)
T80 = 200h